

A fast radio burst localized to a massive galaxy

V. Ravi^{1,2*}, M. Catha³, L. D'Addario¹, S. G. Djorgovski¹, G. Hallinan¹, R. Hobbs³, J. Kocz¹, S. R. Kulkarni¹, J. Shi¹, H. K. Vedantham^{1,4}, S. Weinreb¹ & D. P. Woody³

Intense, millisecond-duration bursts of radio waves (named fast radio bursts) have been detected from beyond the Milky Way¹. Their dispersion measures—which are greater than would be expected if they had propagated only through the interstellar medium of the Milky Way—indicate extragalactic origins and imply contributions from the intergalactic medium and perhaps from other galaxies². Although several theories exist regarding the sources of these fast radio bursts, their intensities, durations and temporal structures suggest coherent emission from highly magnetized plasma^{3,4}. Two of these bursts have been observed to repeat^{5,6}, and one repeater (FRB 121102) has been localized to the largest star-forming region of a dwarf galaxy at a cosmological redshift of 0.19 (refs. 7–9). However, the host galaxies and distances of the hitherto non-repeating fast radio bursts are yet to be identified. Unlike repeating sources, these events must be observed with an interferometer that has sufficient spatial resolution for arcsecond localization at the time of discovery. Here we report the localization of a fast radio burst (FRB 190523) to a few-arcsecond region containing a single massive galaxy at a redshift of 0.66. This galaxy is different from the host of FRB 121102, as it is a thousand times more massive, with a specific star-formation rate (the star-formation rate divided by the mass) a hundred times smaller.

We detected the fast radio burst (FRB) 190523 on 23 May 2019 (modified Julian date (MJD) 58626.254118233(2)), using the Deep Synoptic Array ten-antenna prototype (DSA-10; see Methods). (Throughout this paper, we quote standard errors (68% confidence limits) of the least-significant figures in parentheses.) The DSA-10 consists of 4.5-m radio dishes separated by 6.75 m to 1,300 m, located at the Owens Valley Radio Observatory. The DSA-10 is designed to detect FRBs in the phase-incoherent combination of signals from each dish, and then to process the same signals interferometrically (coherent combination) to localize FRBs to few-arcsecond accuracy. FRB 190523 was detected at a dispersion measure of 760.8(6) pc cm⁻³, and localized to the following J2000 coordinates: right ascension (RA) 13 h 48 min 15.6(2) s; declination (dec.) +72° 28' 11(2)". A time-frequency dataset was formed at this position through the coherent addition of interferometric visibility data from DSA-10 (see Methods). These data, displayed in Fig. 1, consist of total-intensity spectra recorded in 1,250 frequency channels between 1,334.69 MHz and 1,487.28 MHz over 131.072- μ s intervals, with the data in each channel incoherently corrected with at least 8.192- μ s accuracy for the dispersive delay. The burst signal-to-noise ratio exceeds 10 in multiple time samples. The observed properties of FRB 190523 are summarized in Table 1. We derive a fluence of approximately 280 Jy ms given the sensitivity of DSA-10 at the burst location within the field of view. We detected no repeat bursts at this position during approximately 78 h of observations obtained over 54 days surrounding the detection (see Methods).

The 99% confidence containment region of FRB 190523 (Fig. 2) includes just one galaxy in archival data from the Panoramic Survey Telescope and Rapid Response System (Pan-STARRS) 3 π Steradian Survey¹⁰. This galaxy, PSO J207.0643 + 72.4708 (hereafter PSO J207 + 72), was detected with an *r*-band magnitude of 22.1(1) in

the stacked Pan-STARRS data. We obtained images of the containment region of the burst on MJD 58635 with the Keck I telescope of the W. M. Keck Observatory, using the Low Resolution Imaging Spectrometer (KeckI/LRIS; see Methods)¹¹. We detected no objects other than PSO J207 + 72 within the FRB 190523 99% confidence containment region, to limiting magnitudes of 25.8 in the *g*-filter and 26.1 in the *R*-filter. The containment region lies within an apparent grouping of galaxies (Fig. 2), with the galaxy nearest to the containment region (S2 in Fig. 2) having been detected by Pan-STARRS with an *r*-band magnitude of 22.1(1). We also obtained a low-resolution optical spectrum of PSO J207 + 72 using KeckI/LRIS on MJD 58635 (see Methods).

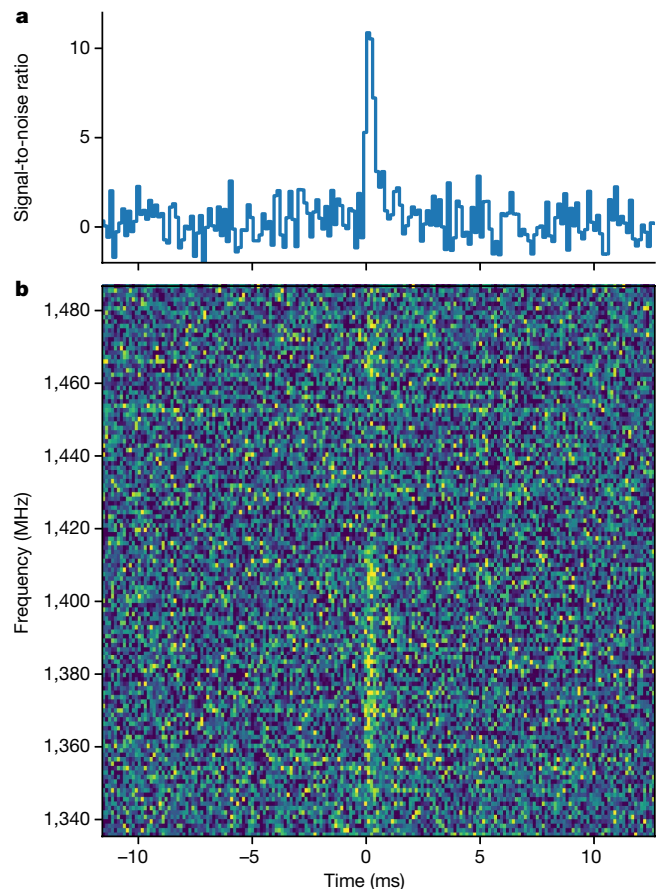


Fig. 1 | Time-frequency data on FRB 190523. a, Dedispersed temporal profile of the burst, averaged over the DSA-10 frequency band. The data are measures of the received power in 131.072- μ s bins, in units of the root-mean-square (r.m.s.) off-burst signal-to-noise ratio. **b**, The dedispersed dynamic spectrum of the burst, again in units of the r.m.s. off-burst signal-to-noise ratio in each 1.22 MHz frequency channel. Although the structure evident in the burst spectrum is probably qualitatively accurate, no calibration of the relative flux density scales in different frequency channels has been applied.

¹Cahill Center for Astronomy and Astrophysics, California Institute of Technology, Pasadena, CA, USA. ²Center for Astrophysics, Harvard and Smithsonian, Cambridge, MA, USA. ³Owens Valley Radio Observatory, California Institute of Technology, Big Pine, CA, USA. ⁴ASTRON, Netherlands Institute for Radio Astronomy, Dwingeloo, The Netherlands. *e-mail: vikram@caltech.edu

Table 1 | Properties of FRB 190523 and its host galaxy

Property	Measurement
Topocentric arrival time at 1,530 MHz (MJD)	58626.254118233(2)
Fluence (Jy ms)	Greater than roughly 280
Dispersion measure (pc cm ⁻³)	760.8(6)
Dispersion measure index	-2.003(8)
Milky Way disk (halo) dispersion measure (pc cm ⁻³)	37 (50 to 80)
Extragalactic dispersion measure (pc cm ⁻³)	644 to 674
Band averaged full-width half-maximum of the burst (ms)	0.42(5)
Scattering timescale at 1 GHz (ms)	1.4(2)
Right ascension (J2000)	13 h 48 min 15.6(2) s
Declination (J2000)	+72° 28' 11(2)''
Host galaxy redshift	0.660(2)
Host galaxy luminosity distance (Gpc)	4.08(1)
Burst spectral energy (erg Hz ⁻¹)	5.6×10^{33}
Host galaxy stellar mass (M_{\odot})	$10^{11.07(6)}$
Host galaxy star-formation rate ($M_{\odot} \text{ yr}^{-1}$)	Less than 1.3(2)

The spectrum (Fig. 3) indicates stellar absorption features at a redshift of 0.660(2). A single emission line, corresponding to the [O II] 3,727-Å doublet, is tentatively detected with a flux of $4.7(7) \times 10^{-17} \text{ erg s}^{-1} \text{ cm}^{-2}$.

We modelled the Pan-STARRS optical photometry and the KeckI/LRIS optical spectroscopy of PSO J207 + 72 using the Prospector software^{12,13}. We used this software to fit a ‘delay-tau’ stellar population and star-formation-history model to the data. In this model, the star-formation history is proportional to $t e^{-t/\tau}$, where t is the time since the formation epoch of the galaxy, and τ is the characteristic decay time of the star-formation history. We derive a metallicity fraction of 0.3(2) of the Solar metallicity, a stellar mass of $10^{11.07(6)} M_{\odot}$ (where M_{\odot} is the mass of the Sun), and an ongoing star-formation rate of approximately $1.3 M_{\odot} \text{ yr}^{-1}$. The star-formation rate—although poorly constrained given the limited wavelength coverage of the data—is consistent with the flux of the possible [O II] 3,727-Å emission line, which implies a star-formation rate of up to $1.3(2) M_{\odot} \text{ yr}^{-1}$ (ref. 14). As this emission line could also be associated with weak activity of the central black hole¹⁵, we adopt a star-formation rate of $1.3(2) M_{\odot} \text{ yr}^{-1}$ as an approximate upper limit for PSO J207 + 72.

As the only object detected within the containment region of FRB 190523, PSO J207 + 72 is the likely host galaxy of the burst. Additional evidence is furnished by the agreement between the burst dispersion measure and the predicted dispersion measure for the redshift of PSO J207 + 72. Accounting for 37 pc cm⁻³ from the Milky Way disk¹⁶, and between 50 pc cm⁻³ and 80 pc cm⁻³ from the Milky Way ionized halo¹⁷, the extragalactic dispersion measure of FRB 190523 is between 644 pc cm⁻³ and 674 pc cm⁻³. Given this extragalactic dispersion measure, and parameterizing the containment region by the $3 \times 8 \text{ arcsec}$ 95% confidence ellipse¹⁸, the probability of finding any galaxy (even one not detectable in our data) by chance within the containment region is less than 10% (ref. 18). Further, the redshift of PSO J207 + 72 is not larger than would be expected given the dispersion measure of FRB 190523. The dispersion measure contributed by the intergalactic medium (IGM) to the redshift of PSO J207 + 72 is $660(f_{\text{IGM}}/0.7) \text{ pc cm}^{-3}$, where f_{IGM} is the fraction of the luminous matter (termed baryons) of the Universe in the ionized IGM¹⁹. Observations suggest that 60% of cosmic baryons are in the IGM (f_{IGM} equals approximately 0.6(1)), 10% of baryons are locked in galaxies, and the remaining 30% of baryons are apportioned between the circumgalactic medium in galaxy halos and the IGM²⁰. We adopt $f_{\text{IGM}} = 0.7$ as a fiducial value, noting that a root-mean-squared scatter of roughly 200 pc cm⁻³ in the IGM dispersion measure to redshifts of around 0.66

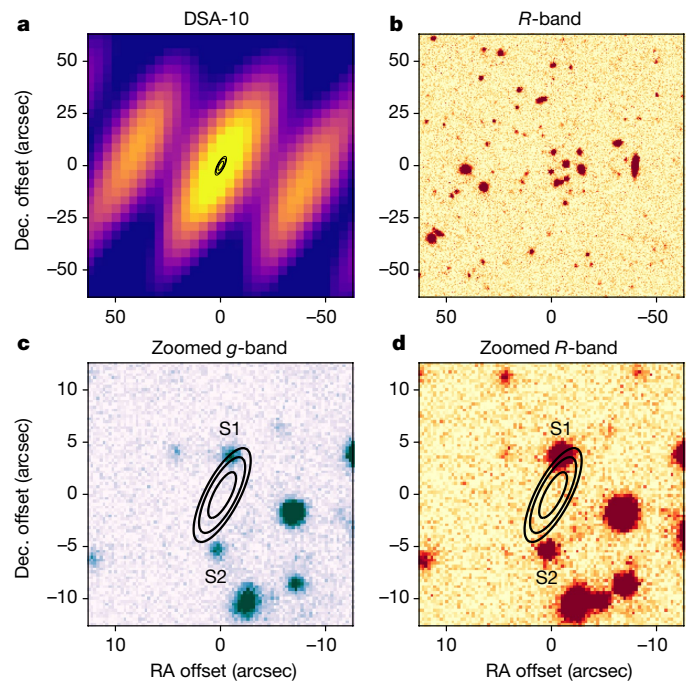


Fig. 2 | Images of the sky location of FRB 190523. All images are centred on J2000 coordinates RA 13 h 48 min 15.6(2) s; dec. +72° 28' 11(2)''.

a, Dirty snapshot image of the burst, obtained with DSA-10 (see Methods).

b, Optical image in the R-band filter, obtained with KeckI/LRIS. The position of FRB 190523 coincides with an apparent grouping of galaxies.

c, d, Zoom-in on the burst localization region in the g- and R-filters of KeckI/LRIS. The position of FRB 190523 is indicated with 68%, 95% and 99% confidence containment ellipses in **a, c, d**. The only galaxy detected above the 26.1-magnitude R-band detection limit within the 99% confidence containment ellipse, indicated by S1, is PSO J207+72. A galaxy to the south of the 99% confidence ellipse is labelled S2.

is expected owing to cosmic variance and intervening galaxy halos²¹. Finally, our R-band KeckI/LRIS image excludes the possibility that the FRB 190523 containment region includes a dwarf galaxy like the host of the repeating FRB 121102 at a redshift below approximately 0.45 (corresponding to a luminosity distance of 2.5 gigaparsecs)⁹. The less than 10% probability of chance coincidence of the burst containment region with a galaxy—even one as small as the FRB 121102 host—implies that there is a less than 10% probability that the FRB 190523 containment region includes a galaxy like the FRB 121102 host. This further suggests that PSO J207 + 72 is the unique host galaxy of FRB 190523.

The properties of FRB 190523 are typical of FRBs observed at frequencies of around 1.4 GHz (ref. 22). At the distance of PSO J207 + 72, FRB 190523 has a spectral energy of $5.6 \times 10^{33} \text{ erg Hz}^{-1}$, which is consistent with the largest previously estimated burst energies²³. The patchy spectrum of FRB 190523 (Fig. 1) is also similar to the spectra of bright FRBs detected by the Australian Square Kilometre Array Pathfinder²³. We note that our DSA-10 observations cannot exclude the possibility of repeated bursts from FRB 190523 below our detection threshold, which FRB 190523 itself exceeded by only 15%.

The temporal profile of FRB 190523 indicates a broadening timescale, owing to multipath propagation through inhomogeneous plasma, of 1.4(2) ms at 1 GHz (ref. 22). This broadening timescale is three orders of magnitude higher than expected for the sightline of FRB 190523 through the Milky Way interstellar medium¹⁶. The broadening timescale is also larger than would be expected during propagation through the dispersion-measure column potentially contributed by PSO J207 + 72 (less than roughly 150 pc cm⁻³)²⁴. Our results therefore support the possibility of some FRBs being temporally broadened during propagation between their host galaxies and the Milky Way, for example, in the circumgalactic medium of intervening galaxies²⁵.

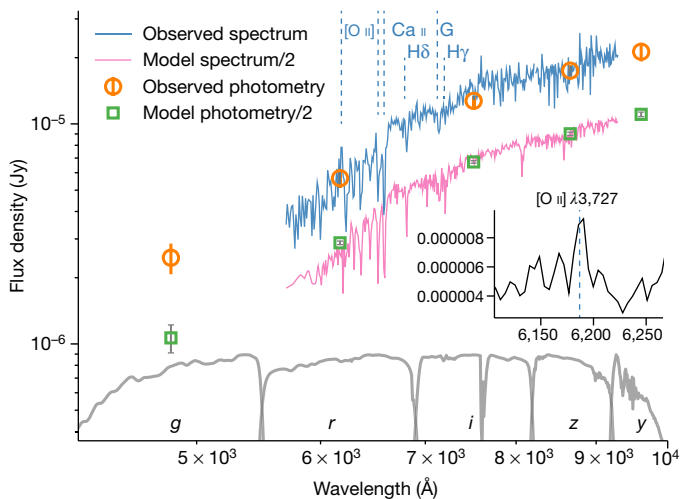


Fig. 3 | Modelling of the host galaxy of FRB 190523. We obtained a low-resolution optical spectrum (blue line) of PSO J207 + 72 using KeckI/LRIS on MJD 58635 (see Methods). We also modelled the Pan-STARRS optical photometry (orange circles) and the KeckI/LRIS optical spectroscopy of PSO J207 + 72 using Prospector software^{12,13} (pink line). Error bars denoting one standard deviation are shown for the Pan-STARRS photometry. The maximum a posteriori probability (MAP) results from the Prospector modelling of the host galaxy are scaled downwards by a factor of two. The grey curves illustrate transmissions from the Pan-STARRS *g*-, *r*-, *i*-, *z*- and *y*-filters. The grey error bars accompanying the MAP photometry points (green boxes) indicate the 5th and 95th percentiles of 500 samples drawn from the posterior parameter distributions. The redshifted positions of some notable absorption lines are indicated by dashed blue traces. The inset shows the observed spectrum around the [O II] 3,727-Å feature, binned by a factor of two less than the spectrum in the main panel.

The properties of PSO J207 + 72 are in tension with FRB progenitor models developed on the basis of the host galaxy of the repeating FRB 121102 (ref. ²⁶). In particular, the host of FRB 121102 is similar to the dwarf-star-forming host galaxies of superluminous supernovae and long gamma-ray bursts, which are the terminal explosions of the most massive stars. However, the stellar mass of PSO J207 + 72 is higher and its star-formation rate per unit mass is lower than those of the known host galaxies of superluminous supernovae and long gamma-ray bursts at redshifts below 1 (ref. ²⁶). In addition, leading models for the FRB emission mechanism favour neutron-star progenitors with magnetar magnetic-field strengths (of greater than roughly 10^{14} G)^{3,4,27}. If this is the case, then our results suggest that magnetars that were formed in the terminal explosions of the most massive stars are not the only objects capable of emitting FRBs. Indeed, magnetar-formation channels exist that do not require young stellar populations, such as the accretion-induced collapse of white dwarfs to neutron stars in mass-transfer binaries^{28,29}, and the merger of two neutron stars³⁰.

The likely low contribution of PSO J207 + 72 to the dispersion measure of FRB 190523 provides evidence in support of FRB progenitor models (magnetar or otherwise) that do not require actively star-forming environments. The low global star-formation rate of PSO J207 + 72, together with the spatially offset location of much of the containment region of FRB 190523 relative to the galaxy (Fig. 2), leads us to consider the possibility that the progenitor of FRB 190523 was drawn from an old stellar population. The similarity between the stellar populations of PSO J207 + 72 and the Milky Way suggests that galaxies like the Milky Way can harbour FRB progenitors.

Online content

Any methods, additional references, Nature Research reporting summaries, source data, extended data, supplementary information, acknowledgements,

peer review information; details of author contributions and competing interests; and statements of data and code availability are available at <https://doi.org/10.1038/s41586-019-1389-7>.

Received: 11 June 2019; Accepted: 25 June 2019;

Published online 2 July 2019.

- Lorimer, D. R., Bailes, M., McLaughlin, M. A., Narkevic, D. J. & Crawford, F. A bright millisecond radio burst of extragalactic origin. *Science* **318**, 777–780 (2007).
- Petroff, E., Hessels, J. W. T. & Lorimer, D. R. Fast radio bursts. *Astron. Astrophys. Rev.* **27**, 4 (2019).
- Kumar, P., Lu, W. & Bhattacharya, M. Fast radio burst source properties and curvature radiation model. *Mon. Not. R. Astron. Soc.* **468**, 2726–2739 (2017).
- Metzger, B. D., Margalit, B. & Sironi, L. Fast radio bursts as synchrotron maser emission from decelerating relativistic blast waves. *Mon. Not. R. Astron. Soc.* **485**, 4091–4106 (2019).
- Spitler, L. et al. A repeating fast radio burst. *Nature* **531**, 202–205 (2016).
- The CHIME/FRB Collaboration. A second source of repeating fast radio bursts. *Nature* **566**, 235–238 (2019).
- Chatterjee, S. et al. A direct localization of a fast radio burst and its host. *Nature* **541**, 58–61 (2017).
- Marcote, B. et al. The repeating fast radio burst FRB 121102 as seen on milliarcsecond angular scales. *Astrophys. J.* **834**, L8 (2017).
- Bassa, C. et al. FRB 121102 is coincident with a star-forming region in its host galaxy. *Astrophys. J.* **843**, L8 (2017).
- Chambers, K. C. et al. The Pan-STARRS1 surveys. Preprint at <https://arxiv.org/abs/1612.05560> (2016).
- Oke, J. B. et al. The Keck low-resolution imaging spectrometer. *Publ. Astron. Soc. Pacif.* **107**, 375–385 (1995).
- Leja, J. & Johnson, B. D. *bd-j/prospector: initial release*. Zenodo <https://doi.org/10.5281/zenodo.1116491> (2017).
- Leja, J., Johnson, B. D., Conroy, C., van Dokkum, P. G. & Byler, N. Deriving physical properties from broadband photometry with prospector: description of the model and a demonstration of its accuracy using 129 galaxies in the local Universe. *Astrophys. J.* **837**, 170 (2017).
- Rosa-González, D., Terlevich, E. & Terlevich, R. An empirical calibration of star formation rate estimators. *Mon. Not. R. Astron. Soc.* **332**, 283–295 (2002).
- Yan, R. et al. On the origin of [O II] emission in red-sequence and poststarburst galaxies. *Astrophys. J.* **648**, 281–298 (2006).
- Cordes, J. M. & Lazio, T. J. W. NE2001. I. A new model for the galactic distribution of free electrons and its fluctuations. Preprint at <http://arxiv.org/abs/astro-ph/0207156> (2002).
- Prochaska, J. X. & Zheng, Y. Probing galactic haloes with fast radio bursts. *Mon. Not. R. Astron. Soc.* **485**, 648–665 (2019).
- Eftekhari, T. & Berger, E. Associating fast radio bursts with their host galaxies. *Astrophys. J.* **849**, 162 (2017).
- Shull, J. M. & Danforth, C. W. The dispersion of fast radio bursts from a structured intergalactic medium at redshifts $z < 1.5$. *Astrophys. J.* **852**, L11 (2018).
- Shull, J. M., Smith, B. D. & Danforth, C. W. The baryon census in a multiphase intergalactic medium: 30% of the baryons may still be missing. *Astrophys. J.* **759**, 23 (2012).
- McQuinn, M. Locating the “missing” baryons with extragalactic dispersion measure estimates. *Astrophys. J.* **780**, L33 (2014).
- Ravi, V. The observed properties of fast radio bursts. *Mon. Not. R. Astron. Soc.* **482**, 1966–1978 (2019).
- Shannon, R. M. et al. The dispersion-brightness relation for fast radio bursts from a wide-field survey. *Nature* **562**, 386–390 (2018).
- Bhat, N. D. R., Cordes, J. M., Camilo, F., Nice, D. J. & Lorimer, D. R. Multifrequency observations of radio pulse broadening and constraints on interstellar electron density microstructure. *Astrophys. J.* **605**, 759–783 (2004).
- Vedantham, H. K. & Phinney, E. S. Radio wave scattering by circumgalactic cool gas clumps. *Mon. Not. R. Astron. Soc.* **483**, 971–984 (2019).
- Metzger, B. D., Berger, E. & Margalit, B. Millisecond magnetar birth connects FRB 121102 to superluminous supernovae and long-duration gamma-ray bursts. *Astrophys. J.* **841**, 14 (2017).
- Lyutikov, M. Coherence constraints on physical parameters at bright radio sources and FRB emission mechanism. Preprint at <https://arxiv.org/abs/1901.03260> (2019).
- Piro, A. L. & Kollmeier, J. A. Ultrahigh-energy cosmic rays from the “en caul” birth of magnetars. *Astrophys. J.* **826**, 97 (2016).
- Ruiter, A. J. et al. On the formation of neutron stars via accretion-induced collapse in binaries. *Mon. Not. R. Astron. Soc.* **484**, 698–711 (2019).
- Giacomazzo, B. & Perna, R. Formation of stable magnetars from binary neutron star mergers. *Astrophys. J.* **771**, L26 (2013).

Publisher's note: Springer Nature remains neutral with regard to jurisdictional claims in published maps and institutional affiliations.

© The Author(s), under exclusive licence to Springer Nature Limited 2019

METHODS

The DSA-10 instrument. The Deep Synoptic Array 10-element prototype (DSA-10) is an array of ten 4.5-m radio dishes operating in the frequency band 1.28–1.53 GHz. The array is deployed at the Owens Valley Radio Observatory (OVRO; located at 37.2314°N, 118.2941°W) near the town of Bishop, California, USA. A description of the DSA-10 instrument is given in ref. ³¹. Here we describe the state of the instrument at the time that FRB 190523 was detected.

The array was in a slightly modified configuration relative to its initial deployment, with four antennas clustered at the northern end of the OVRO T-shaped infrastructure. The positions of each antenna, in standard International Terrestrial Reference Frame (ITRF) geocentric coordinates, are given in Extended Data Table 1. Each antenna was equipped with two receivers sensitive to orthogonal linear polarizations. The antenna primary beams have full-width half-maxima of 3.25°. Antenna 2 was not operational because it was being used to test new equipment, and one polarization of antenna 8 was operating with substantially reduced sensitivity caused by a malfunctioning low-noise amplifier. Antenna 2 was discarded from all calibration and imaging procedures described below. The array operated in a stationary drift-scan mode on the meridian at a declination of +73.6°, with an absolute pointing accuracy of better than 0.4°. The projected baseline lengths ranged between 5.75 m and 1,256.57 m.

The DSA-10 was operated in this configuration between MJD 58568 and MJD 58630, with a total time on-sky of 54 days. FRB searching was conducted using the incoherent sum of dynamic spectra from the eight fully functioning antennas, forming a single stream of 2,048-channel spectra integrated over 131.072 μ s. Before summation, the dynamic spectra were excised of narrow-band and impulsive broadband radio-frequency interference (RFI)³¹. We searched these data for FRBs in real time using the Heimdall software³², with 2,477 optimally spaced dispersion-measure trials between 30 pc cm⁻³ and 3,000 pc cm⁻³. At each trial dispersion measure, the data were smoothed with boxcar filters spaced by powers of two between 2⁰ and 2⁸ samples before searching. The detection threshold was set at eight standard deviations (8 σ). In this study, we assume a typical band-averaged system-equivalent flux density of 22 kJy for each DSA-10 receiver, on the basis of interferometric measurements of the system sensitivity using sources with known flux densities³¹. Given eight fully functioning antennas, and 220 MHz of effective bandwidth following RFI excision, this implies an approximate detection threshold of 94 Jy ms at the centre of the primary beam for a millisecond-duration FRB not affected by intrachannel dispersion smearing³³.

Upon detection of any pulse candidate that exceeded the detection threshold at any trial dispersion measure, 294,912 samples of complex voltage data corresponding to each polarization of each antenna were written to disk. These data consisted of 4-bit real, 4-bit imaginary 2,048-channel voltage spectra sampled every 8.192 μ s, calculated on and transmitted to five servers by Smart Network ADC Processor (SNAP-1) boards³⁴ over a 10-gigabit ethernet network. The data dumps were extracted from ring buffers such that the candidate pulse arrival times at 1,530 MHz were 61,035 samples into the dumps.

These voltage data were also used to derive interferometric visibilities between each pair of antennas. The visibilities were measured by integrating the cross-power over 0.402653184 s, and over 625 pairs of channels between exactly 1,334.6875 MHz and 1,487.275390625 MHz. Approximate, constant-path-length delay corrections were digitally applied to each receiver input on the SNAP-1 boards, but no time-dependent fringe-tracking corrections were applied online. Visibility data were recorded only when bright unresolved radio sources were transiting through the DSA-10 primary beam. These data were fringe-stopped offline by dividing the data by a model for the visibilities given the known source positions from the National Radio Astronomy Observatory (NRAO) Very Large Array (VLA) Sky Survey (NVSS) catalogue³⁵. Visibility modelling was accomplished using differential antenna positions referenced to the known ITRF location of the centre of the OVRO T-shape (which had previously hosted the Caltech OVRO Millimeter Array), using the Common Astronomy Software Applications (CASA, version 5.1.1) package to calculate baseline coordinates. We consider visibility data on three such sources here: NVSS J120019 + 730045 (also 3C 268.1, 5.56 Jy; hereafter J1200 + 7300), NVSS J145907 + 714019 (7.47 Jy; hereafter J1459 + 7140) and NVSS J192748 + 735802 (3.95 Jy; hereafter J1927 + 7358). Data on these sources were recorded for 3,630 s, 1,960 s and 3,890 s, respectively, centred on their transit times.

Interferometric calibration and localization of FRB 190523. We used standard strategies for processing radio-interferometric data³⁶ to calibrate the instrumental responses of each DSA-10 antenna and receiver. Here we describe the specific methods used to calibrate the data on FRB 190523, and the steps taken to verify their efficacy.

FRB 190523 was detected on MJD 58626.254118233(2), and a voltage-data dump was successfully triggered. These data were cross-correlated offline using the same routines as applied in the online correlator software³⁷, and the visibilities were

integrated over 131.072 μ s. Only data in 1,250 channels covering the frequency band (1,334.6875–1,487.275390625 MHz) spanned by the visibility data recorded in real time were retained in the analysis presented here.

At the time FRB 190523 was detected, the DSA-10 pointing centre was at a position (J2000) of RA 14 h 15 min 01.98 s, dec. +73° 40' (absolute pointing accuracy of better than 0.4°). The calibrator sources J1459 + 7140 and J1200 + 7300 transited 29.58 min later and 163.76 min earlier, respectively. The phases of the per-receiver complex gain corrections for the FRB 190523 data were derived as follows. No attempt at per-receiver gain amplitude calibration was made. This was because all sources under consideration (including FRB 190523) were consistent with unresolved point sources, based on NVSS data³⁵, that dominated the sky brightness within their fields. All visibility amplitudes were taken to be unity, such that only phase information was preserved.

First, receiver-based relative delay errors (with antenna 7 as a reference) were calculated using fringe-stopped data on J1459 + 7140, restricted to the 15 min surrounding transit. J1459 + 7140 is considered to be a primary calibrator in the database of the VLA for baseline lengths consistent with the DSA-10.

Second, after applying these delay corrections to the 15 min of J1459 + 7140 data surrounding transit, the data were averaged in time, and in frequency to 25 channels. The averaged data were used to derive receiver-based phase errors in each channel.

Third, the phase solutions from J1459 + 7140 were averaged with phase solutions derived from 15 min of fringe-stopped data on J1200 + 7300 surrounding transit, with the same delay corrections as above applied first. No substantial differences were evident between the phase solutions derived independently from J1459 + 7140 and J1200 + 7300.

Fourth, the delay and phase solutions from the above analysis were used to calibrate the visibility data on FRB 190523. The phase centre was set to the array pointing centre at the time of the burst. The data were converted to the measurement-set format for further analysis with CASA. Data on the four shortest baselines (after removing baselines with antenna 2) were excluded because of substantial levels of correlated noise. A 7° × 7° total-intensity image, without deconvolution of the synthesized beam shape (a 'dirty' image), was then made using four visibility time-samples centred on the burst, with the standard imaging task `tclean` applied for gridding and Fourier inversion. A single point-like source was evident in this image, at a position 2.3° from the pointing centre (an hour angle of 26.8' west and 1.2° south).

Fifth, given the apparent offset location of the burst from the pointing centre, we then corrected for any direction-dependent instrumental-response variations intrinsic to the DSA-10 antennas. This was done by extracting 6 min of fringe-stopped data on J1200 + 7300 at the same hour angle as the possible position of FRB 190523, applying the previous calibration solutions, and deriving frequency-averaged phase corrections for each receiver (again using antenna 7 as a reference). We note that no data on J1459 + 7140 were available at the hour angle of the burst, as visibilities were recorded on this source for a shorter time (1,960 s) than for J1200 + 7300 (3,630 s). Large corrections of up to 25° in phase were required, which were identical for the two receivers on each antenna. This formed the final set of calibration solutions for FRB 190523.

We then applied these final calibration solutions to the visibility data on FRB 190523, and referenced the data to a phase centre corresponding to the approximate burst position, with the burst dispersion accounted for in calculating baseline coordinates. The data were then summed over the two polarizations, and converted to the measurement-set format. The CASA task `tclean` was used to make dirty and deconvolved images of the burst data (see Fig. 2 and the bottom row of Extended Data Fig. 1). The imaging process was verified using the 6 min of data on J1200 + 7300 obtained at the same hour angle as FRB 190523 (Extended Data Fig. 1, top row). No sources were detected in images made using visibility data in 128 time samples on either side of FRB 190523, either when averaged together or when binned by four samples.

The position of FRB 190523 was estimated by fitting to the calibrated visibilities, using four 131.072- μ s time samples centred on the burst, as before. This fit was carried out using the MIRIAD³⁸ task `uvfit` (after converting the measurement set to a MIRIAD-format file) and a grid-search code, as a software problem in the CASA task `uvmodellfit` prevented it from loading our data. The grid-search code was used to evaluate the posterior probability of the source position given the likelihood of the visibility data over a uniform 0.25-arcsec grid of positions centred on the burst position in its image. This was then used to calculate the maximum a posteriori probability location quoted in Table 1, and the 68%, 95% and 99% confidence containment ellipses shown in Fig. 2. We also attempted to estimate the position of FRB 190523 using only data between 1,350 MHz and 1,420 MHz, where much of the burst spectral energy density appears to be concentrated (Fig. 1). This yielded a containment ellipse that was consistent with the result from all the data, but with major and minor axes that were 10% larger.

We verified the efficacy of our localization procedure using a selection of methods. First, no substantial phase closure errors were evident in the calibrated data on J1200 + 7300 and J1459 + 7140, either at boresight, or at the hour angle of FRB 190523 in the case of J1200 + 7300. No baseline-based calibration corrections were required to accurately model the calibrator data. Second, we verified that the calibration solutions derived as above for FRB 190523 were also able to calibrate visibility data on the source J1927 + 7358, which transited five hours after the burst detection. We did this by extracting 6 min of data on J1927 + 7358 at the hour angle that the burst was detected, applying the same calibration solutions as applied to the burst, and imaging it and deriving its position as for the burst (Extended Data Fig. 1, middle row). The position of J1927 + 7358 was recovered to within 1 arcsec in both dimensions, with the offsets consistent with the position-fit errors. Plots of the calibrated, frequency-averaged visibility phases on each baseline of 6 min of data on J1200 + 7300 and J1927 + 7358 after rotation to their known positions are shown in Extended Data Fig. 2, together with the same results for FRB 190523 rotated to its derived position. The single worst outliers in Extended Data Fig. 2 for FRB 190523 and J1927 + 7358 were both on baselines containing antenna 1.

We repeated the same calibration procedure as above on the 12 days of data before detection of the burst, and correctly recovered the position of J1927 + 7358 on each day (Extended Data Fig. 3). The r.m.s. scatter in the recovered positions of J1927 + 7358 about the true value was 0.47 arcsec in RA, and 0.69 arcsec in dec. We therefore have no basis to add a systematic-error contribution to the position-fit errors for FRB 190523. We have previously verified that no temporal error existed in the voltage-data dumps by imaging giant pulses from the Crab pulsar (B0531 + 21) when the DSA-10 was pointed at its declination, running the same software³¹. We ensured that this remained the case by calibrating and imaging data dumps obtained close to when J1200 + 7300 was transiting on other days using the above procedures, and verifying that the position of J1200 + 7300 was correctly recovered.

The final astrometric reference for our results was the VLA calibrator catalogue, which was accurate to less than 0.01 arcsec for J1459 + 7140 and J1927 + 7358, and to the NVSS accuracy of approximately 0.5 arcsec (ref. ³⁵) for J1200 + 7300. These errors are small in comparison with the final localization accuracy of FRB 190523, and hence we do not include them in the localization-error budget of the burst.

Properties of FRB 190523. We modelled the temporal profile of FRB 190523 using published methods²². The data presented in Fig. 1 were formed by the coherent addition of calibrated visibility data on FRB 190523 using its best-fit position. These data were integrated over five evenly spaced frequency bands, and the resulting time series were fit with a series of models. The best-fit model was the convolution of the instrumental response to a delta-function impulse and a one-sided exponential with a timescale varying as f^{-4} , where f is the observed frequency. This is consistent with temporal broadening caused by multipath propagation. The extrapolated broadening timescale at 1 GHz is quoted in Table 1. We also quote the uncertainty in the dispersion-measure index in Table 1; we found the burst arrival time to scale with $f^{-2.003(8)}$.

We made no attempt to calibrate the response of the DSA-10 to polarized radiation. The DSA-10 was not designed for polarimetry. First, we have not established our ability to robustly calibrate the per-receiver frequency-dependent gain amplitudes using transiting continuum calibrator sources. We also do not record full-polarization visibility data on these sources, making it impossible to measure signal leakages between the receivers that are sensitive to orthogonal linear polarizations. The lack of polarization information is not likely to affect the burst localization, because each polarization was calibrated independently using unpolarized sources. We verified that consistent positions for FRB 190523 were derived from data in each polarization separately.

KeckI/LRIS observations and analysis. KeckI/LRIS observations of the localization region and candidate host galaxy of FRB 190523 (PSO J207 + 72) were carried out on the night of MJD 58635 in dark time, under clear photometric conditions with a median seeing-disk full-width half-maximum (R -band) of 1.1 arcsec. Light from the telescope was split between the two arms of LRIS by the D560 dichroic. Three images were taken in the g - and R -band filters at an airmass of 1.66, with exposure times of 30 s, 300 s and 300 s, and no binning of the detector pixels. The g - and R -band filters have effective wavelengths of 4,731 Å and 6,417 Å, respectively, and effective widths of 1,082 Å and 1,185 Å, respectively. Three spectral exposures were obtained (with exposure times of 900 s and a median airmass of 1.68) with a 1.5-arcsec long slit at a position angle of 270°, the 600/4,000 grism for the blue arm, the 400/8,500 grating for the red arm, and the detector binned by two pixels in the spectral direction. The spectral-flux calibration was obtained with observations of the standard star Feige 67 at an airmass of 1.07.

All optical data were reduced using standard procedures for LRIS. Bias subtraction using the overscan levels, flat-fielding using dome-flat exposures, and cosmic-ray rejection were performed with *lpipe* software³⁹. The imaging data were then astrometrically registered against Gaia data-release 2 (DR2) stars using *scamp* software routines⁴⁰, co-added using *swarp* software routines⁴¹, and sources were

extracted using the *SExtractor* software⁴². Photometric calibration to an accuracy of 0.1 magnitudes was accomplished using Pan-STARRS objects in the field. The weakest detected sources in the g - and R -bands were 25.8 and 26.1 magnitudes (AB) respectively, which we adopt as our limiting magnitudes in these bands.

We also used the *lpipe* software to process the spectroscopic data by performing wavelength calibration using internal-arc exposures corrected by sky-emission lines, and by optimally subtracting the sky-emission lines. We then performed optimal extraction of the spectral traces in each on-source exposure by using the trace of the standard star Feige 67, which we also used for flux calibration and the removal of telluric absorption lines. The final optimally co-added spectrum of PSO J207 + 72 has a flux calibration uncertainty of 10% owing to the differing air masses of the standard-star and source observations. The galaxy was detected only in the red arm of LRIS, and a truncated spectrum (displayed in Fig. 3) was used for further analysis. In addition to the [O II] 3,727-Å emission-line doublet, some other detected absorption lines (Ca II H and K lines at 3,935 Å and 3,970 Å respectively, H γ at 4,342 Å and H δ at 4,103 Å, and the Fraunhofer G feature at 4,306 Å) are labelled in Fig. 3. All lines were detected at a redshift of 0.660(2).

Modelling of the host galaxy. We modelled the Pan-STARRS photometry and KeckI/LRIS spectrum of PSO J207 + 72 using the *Prospector* code for stellar-population inference. *Prospector* enables Markov Chain Monte Carlo (MCMC) sampling of the posterior distribution of parameters of the stellar populations and star-formation histories of galaxies, given a combination of photometric and spectroscopic data. Galaxy emission is modelled using a wrapper to the flexible stellar-population synthesis code^{43,44}. We fit a five-parameter ‘delay-tau’ model for the stellar population of PSO J207 + 72, including the metallicity, the stellar-population age and star-formation timescale, the mass in formed stars, and the V -band extinction of a dust screen. Before performing the fit, we corrected the observations for Galactic extinction using the ‘*extinction*’ software package⁴⁵, through a standard Milky Way extinction curve with a V -band extinction of 0.052 magnitudes. Data surrounding the detected [O II] 3,727-Å emission-line doublet were masked, and no modelling of nebular emission was conducted. We conducted exploration of the posterior parameter distributions using the *emcee* MCMC software⁴⁶. Standard *Prospector* priors were implemented. We derived a metallicity of 0.3(2) of the solar metallicity, a mass in formed stars of $10^{11.07(6)} M_{\odot}$, an age of 6.6(8) Gyr, a star-formation timescale of 1.0(2) Gyr, and a V -band extinction of 0.3(2) magnitudes.

PSO J207 + 72 lies within what appears to be a group of galaxies (Fig. 2) with Pan-STARRS r -band magnitudes ranging between 19 and 23. No spectra are available at present for galaxies within this group, and the association in distance cannot therefore be confirmed. PSO J207 + 72 is undetected in observations from the VLA Sky Survey⁴⁷; the upper limit at 3 GHz on any source within the 99% confidence containment region of FRB 190523 is 0.36 mJy (3σ). Throughout this paper, we use cosmological parameters from the 2015 Planck analysis⁴⁸.

Data availability

The datasets generated during and/or analysed during this study are available from the corresponding author on reasonable request.

Code availability

Custom code is made available at <https://github.com/VR-DSA>.

- Kocz, J. et al. DSA-10: a prototype array for localizing fast radio bursts. Preprint at <https://arxiv.org/abs/1906.08699> (2019).
- Barsdell, B. R., Bailes, M., Barnes, D. G. & Fluke, C. J. Accelerating incoherent dedispersion. *Mon. Not. R. Astron. Soc.* **422**, 379–392 (2012).
- Cordes, J. M. & McLaughlin, M. A. Searches for fast radio transients. *Astrophys. J.* **596**, 1142–1154 (2003).
- Hickish, J. et al. A decade of developing radio-astronomy instrumentation using CASPER open-source technology. *J. Astron. Instrum.* **5**, 1641001 (2016).
- Condon, J. J. et al. The NRAO VLA Sky Survey. *Astron. J.* **115**, 1693–1716 (1998).
- Thompson, A. R., Moran, J. M. & Swenson, G. W. Jr *Interferometry and Synthesis in Radio Astronomy* 3rd edn (Springer, 2017).
- Clark, M. A., LaPlante, P. C. & Greenhill, L. J. Accelerating radio astronomy cross-correlation with graphics processing units. *Int. J. High Perform. Comput. Appl.* **27**, 178–192 (2013).
- Sault, R. J., Teuben, P. J. & Wright, M. C. H. A retrospective view of MIRIAD. In *Astronomical Data Analysis Software and Systems IV, ASP Conf. Ser.* vol. 77 (eds Shaw, R. A. et al.) 433 (1995).
- Perley, D. A. Fully-automated reduction of longslit spectroscopy with the low resolution imaging spectrometer at Keck Observatory. Preprint at <https://arxiv.org/abs/1903.07629> (2019).
- Bertin, E. Automatic astrometric and photometric calibration with SCAMP. In *Astronomical Data Analysis Software and Systems XV, ASP Conf. Ser.* vol. 351 (eds Gabriel, C. et al.) 112 (2006).
- Bertin, E. et al. The TERAPIX pipeline. In *Astronomical Data Analysis Software and Systems XI, ASP Conf. Proc.* vol. 281 (eds Bohlender, D. A. et al.) 228 (2002).
- Bertin, E. & Arnouts, S. *SExtractor*: software for source extraction. *Astron. Astrophys. Suppl. Ser.* **117**, 393–404 (1996).

43. Conroy, C., Gunn, J. E. & White, M. The propagation of uncertainties in stellar population synthesis modeling. I. The relevance of uncertain aspects of stellar evolution and the initial mass function to the derived physical properties of galaxies. *Astrophys. J.* **699**, 486–506 (2009).
44. Conroy, C. & Gunn, J. E. The propagation of uncertainties in stellar population synthesis modeling. III. Model calibration, comparison, and evaluation. *Astrophys. J.* **712**, 833–857 (2010).
45. Barbary, K. extinction v0.3.0. *Zenodo* <https://doi.org/10.5281/zenodo.804967> (2016).
46. Foreman-Mackey, D., Hogg, D. W., Lang, D. & Goodman, J. emcee: the MCMC hammer. *Publ. Astron. Soc. Pacif.* **125**, 306 (2013).
47. Murphy, D. & Lacy, M. VLA sky survey. <https://science.nrao.edu/science/surveys/vlass> (2019).
48. Planck Collaboration. Planck 2015 results. XIII. Cosmological parameters. *Astron. Astrophys.* **594**, A13 (2016).

Acknowledgements We thank the staff of the Owens Valley Radio Observatory, including J. Lamb, K. Hudson, A. Rizo and M. Virgin, for their assistance with the construction of the DSA-10. We thank A. Readhead for supporting the initiation of the DSA-10 project. We also thank A. Soliman for assistance with the development of the DSA-10 receivers. A portion of this research was performed at the Jet Propulsion Laboratory, California Institute of Technology, under a President and Directors Fund grant and under a contract with the National Aeronautics and Space Administration (NASA). This research was additionally supported by the National Science Foundation (NSF) under grant AST-1836018. V.R. acknowledges support as a Millikan Postdoctoral Scholar in Astronomy at the California Institute of Technology, and from a Clay Postdoctoral Fellowship of the Smithsonian Astrophysical Observatory. S.G.D. acknowledges partial support from NSF grant AST-1815034 and NASA grant 16-ADAP16-Q232. Some of the data presented herein were obtained at the W. M. Keck Observatory, which is operated as a scientific partnership among the California Institute of Technology, the University of California and NASA.

The Observatory was made possible by the financial support of the W. M. Keck Foundation. This research made use of Astropy, a community-developed core Python package for astronomy. The Pan-STARRS1 Surveys (PS1) and the PS1 public science archive have been made possible through contributions by the Institute for Astronomy, the University of Hawaii, the Pan-STARRS Project Office, the Max-Planck Society and its participating institutes, the Max-Planck Institute for Astronomy, Heidelberg, the Max-Planck Institute for Extraterrestrial Physics, Garching, Johns Hopkins University, Durham University, the University of Edinburgh, Queen's University Belfast, the Harvard-Smithsonian Center for Astrophysics, the Las Cumbres Observatory Global Telescope Network Incorporated, the National Central University of Taiwan, the Space Telescope Science Institute, NASA under grant NNX08AR22G issued through the Planetary Science Division of the NASA Science Mission Directorate, NSF grant AST-1238877, the University of Maryland, Eotvos Lorand University, the Los Alamos National Laboratory, and the Gordon and Betty Moore Foundation.

Author contributions G.H., V.R. and H.K.V. conceived of and developed the DSA-10 concept and observing strategy. V.R., J.K. and S.R.K. led the construction and initial deployment of DSA-10. D.P.W., S.W., L.D., J.K., V.R., H.K.V., M.C., R.H. and J.S. designed and built the DSA-10 subsystems. V.R. and H.K.V. commissioned the DSA-10. V.R. operated the DSA-10 and analysed the data. S.G.D. carried out the optical observations. V.R. analysed the optical data, and led the writing of the manuscript with the assistance of all co-authors.

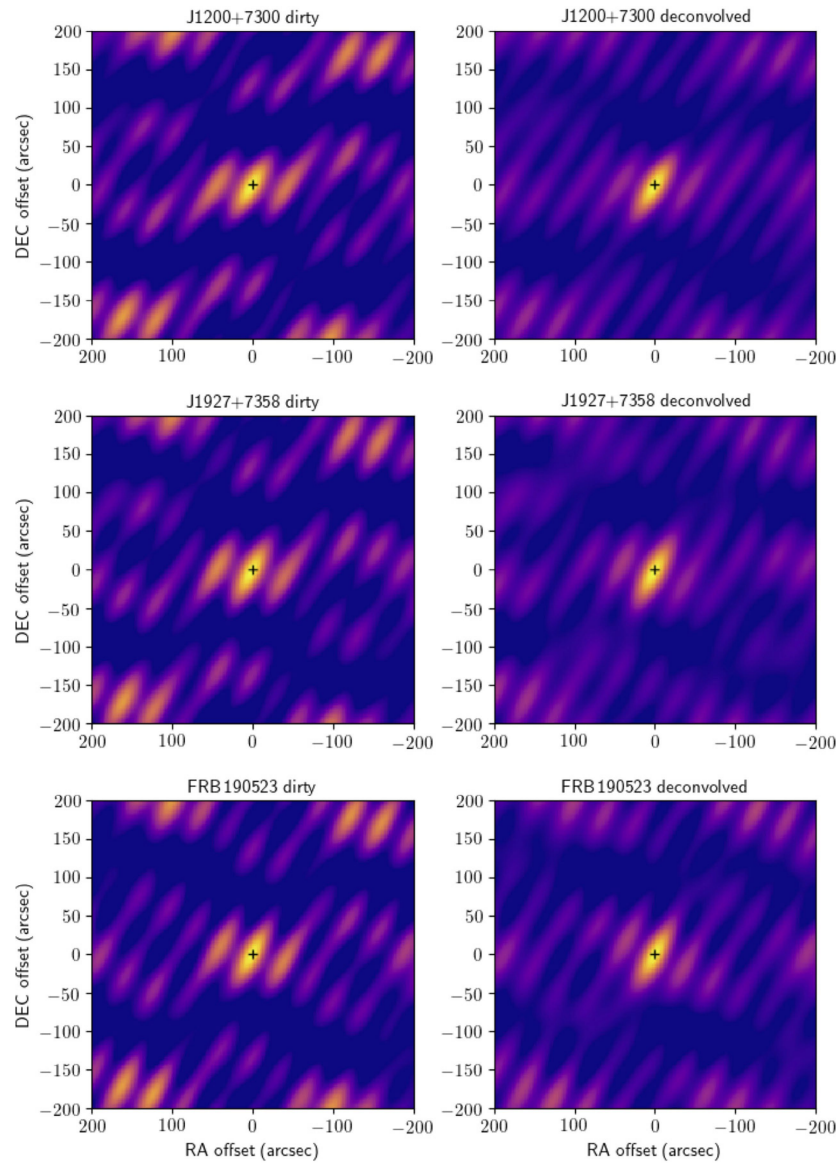
Competing interests : The authors declare no competing interests.

Additional information

Correspondence and requests for materials should be addressed to V.R.

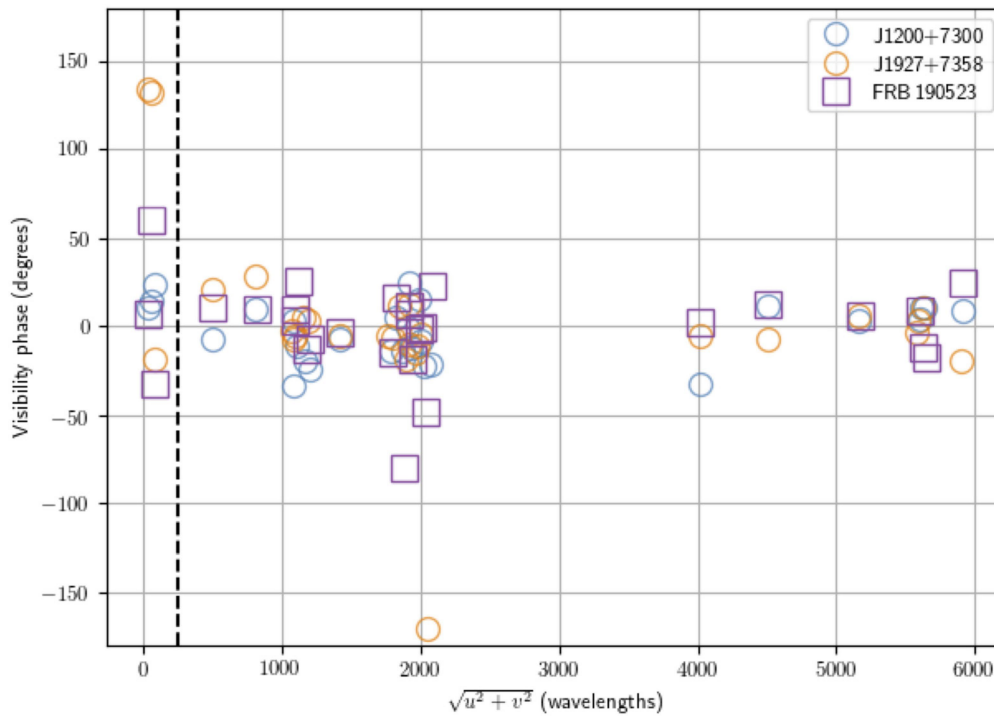
Peer review information *Nature* thanks Shami Chatterjee and Jason Hessels for their contribution to the peer review of this work.

Reprints and permissions information is available at <http://www.nature.com/reprints>.



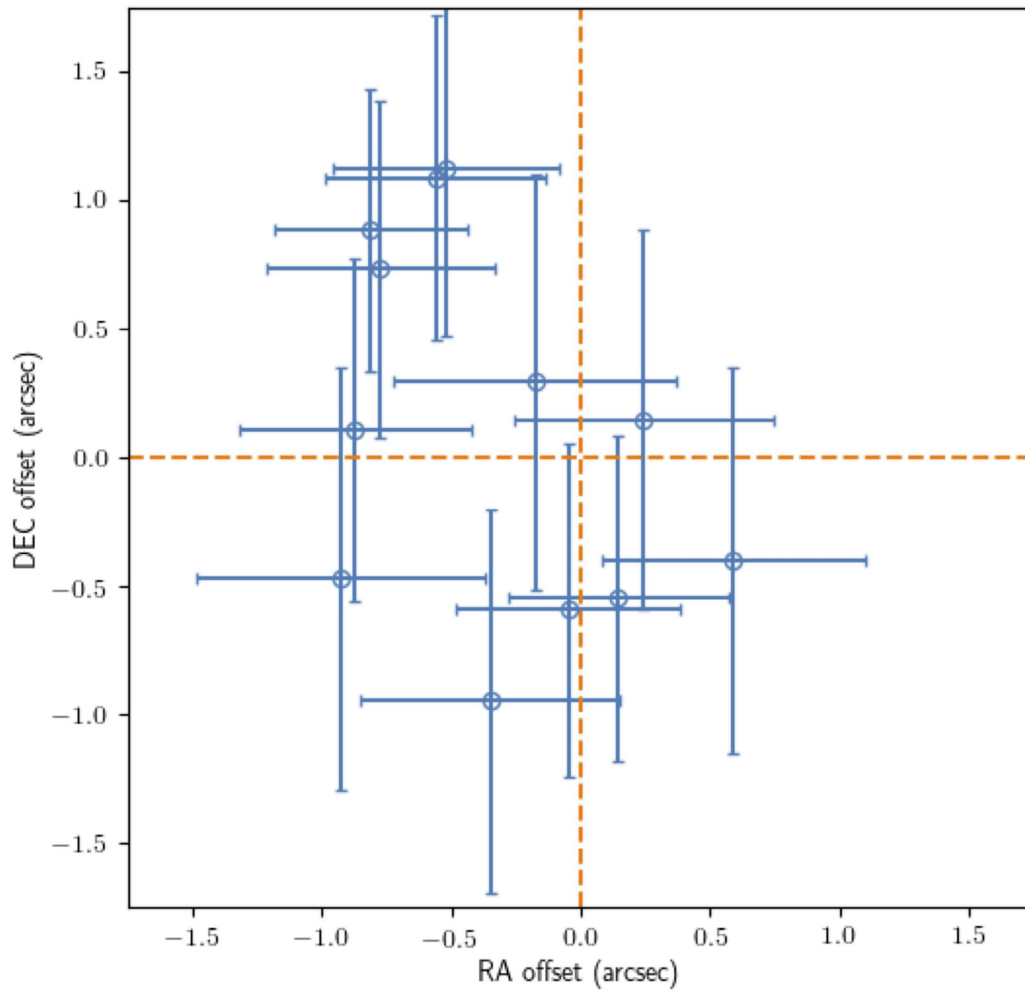
Extended Data Fig. 1 | DSA-10 images. Dirty and deconvolved images are shown of two bright point-sources and FRB 190523. All data were obtained at the same hour angle relative to the meridian, within 12 h of each other. The same calibration solution, derived using the J1200 + 7300 data, was applied to all data. The black crosses indicate the known

source positions in the top and middle rows, and the best-fit position of FRB 190523 in the bottom row. The recovery of the correct position of J1927 + 7358 at the hour angle that FRB 190523 was detected at demonstrates the accuracy of the calibration solutions.



Extended Data Fig. 2 | Visibility phases measured for two bright point-sources and FRB 190523. Only data on baselines including fully functioning antennas are shown. The visibility data were phase-rotated to the known (or best-fit for FRB 190523) source positions, and averaged across the frequency band. Data on the shortest baselines (to the left of the dashed vertical line) were corrupted by correlated noise, and were

discarded from imaging analysis. All data were calibrated using the same calibration solution, which was partially based on the J1200 + 7300 data, and were obtained at the same hour angle relative to the meridian within a 12-h timeframe. The x axis shows the baseline lengths in units of wavelengths at the middle of the DSA-10 frequency band.



Extended Data Fig. 3 | Recovered positions of J1927 + 7358 on 12 separate days. Each position was derived from 5 min of visibility data, extracted when J1927 + 7358 was at the same hour angle as FRB 190523

was detected. On each day, the data were also calibrated in exactly the same way as the FRB 190523 data. The error bars indicate the 68% (1σ) confidence intervals for the estimated positions.

Extended Data Table 1 | ITRF coordinates for the ten DSA-10 antennas

Antenna	X (m)	Y (m)	Z (m)
1	-2409464.509	-4477971.270	3839125.031
2	-2409466.445	-4477974.866	3839119.657
3	-2409470.315	-4477982.059	3839108.908
4	-2409547.552	-4478125.603	3838894.418
5	-2409468.38	-4477978.463	3839114.282
6	-2409429.957	-4478294.47	3838772.061
7	-2409682.474	-4478158.598	3838772.061
8	-2409746.758	-4478124.008	3838772.061
9	-2409770.667	-4478111.143	3838772.061
10	-2410525.007	-4477850.573	3838597.062